Article:

Metman, MC, Livermore, PW orcid.org/0000-0001-7591-6716 and Mound, JE orcid.org/0000-0002-1243-6915 (2018) The reversed and normal flux contributions to axial dipole decay for 1880–2015. Physics of the Earth and Planetary Interiors, 276. pp. 106-117. ISSN 0031-9201

https://doi.org/10.1016/j.pepi.2017.06.007

The reversed and normal flux contributions to axial dipole decay for 1880-2015

M. C. Metman[a,*], P. W. Livermore[a], J. E. Mound[a]

[a] *School of Earth and Environment, University of Leeds, Leeds LS2 9JT, United Kingdom*

Abstract

The axial dipole component of Earth's internal magnetic field has been weakening since at least 1840, an effect widely believed to be attributed to the evolution of reversed flux patches (RFPs). These are regions on the core-mantle boundary (CMB) where the sign of radial flux deviates from that of the dominant sign of hemispheric radial flux. We study dipole change over the past 135 years using the field models gufm1, COV-OBS.x1 and CHAOS-6; we examine the impact of the choice of magnetic equator on the identification of reversed flux, the contribution of reversed and normal flux to axial dipole decay, and how reversed and normal field evolution has influenced the axial dipole. We show that a magnetic equator defined as a null-flux curve of the magnetic field truncated at spherical harmonic degree 3 allows us to robustly identify reversed flux, which we demonstrate is a feature of at least degree 4 or 5. Additionally, our results indicate that the evolution of reversed flux accounts for approximately two-thirds of the decay of the axial dipole, while one third of the decay is attributed to the evolution of the normal field. We find that the decay of the axial dipole over the 20^{th} century is associated with both the expansion and poleward migration of reversed flux. In contrast to this centennial evolution, changes in the structure of secular variation since epoch 2000 indicate that poleward migration currently plays a much reduced role in the ongoing dipole decay.

Keywords: geomagnetism, axial dipole, reversed flux patches, secular variation, magnetic equator

DOI: `10.1016/j.pepi.2017.06.007`

*Corresponding author

Email addresses: `eemcm@leeds.ac.uk` (M. C. Metman), `p.w.livermore@leeds.ac.uk` (P. W. Livermore), `earjem@leeds.ac.uk` (J. E. Mound)

1. Introduction

Observations of Earth's internal magnetic field reveal that its largest component is that of the axial dipole, which has been in decline since at least 1840 by a rate of approximately 15 nT yr^{-1} (Barraclough, 1974; Gubbins, 1987; Gubbins et al., 2006) (see also Fig. 1). The strength of this component is measured by the degree one, order zero spherical harmonic or Gauss coefficient g_1^0 (e.g. Backus et al., 1996). A determination of this component has been possible since Gauss' work in the 1830's and estimates have been refined by modern observatory and satellite data (e.g. Finlay et al., 2016b).

The coefficient g_1^0 can be computed with knowledge of the radial magnetic field B_r on the core-mantle boundary (CMB) through evaluation of the integral:

$$g_1^0(t) = \frac{3c}{8\pi a^3} \int_S B_r(\mathbf{r}, t) \cos\theta \, \mathrm{d}S \tag{1}$$

where t is time, $\mathbf{r}$ is the position vector, a and c are the radii of the Earth and its outer core respectively, θ is colatitude and S is the area of the CMB (Gubbins, 1987). Figure 1 shows the integrand of Eq. (1) evaluated at the CMB at epochs 1840.0 and 2015.0. The integral is negative and therefore so is g_1^0. However, there are regions on the CMB where the integrand is positive, which therefore contribute destructively towards $|g_1^0|$. These regions may be referred to as reversed flux patches (RFPs).

Temporal variation in B_r, and therefore in $|g_1^0|$, ultimately results from the convection of the electrically conducting iron-alloy that comprises the outer core. However, Eq. (1) illustrates that the secular variation of $|g_1^0|$ may be expressed mathematically in terms of B_r at the CMB only. With this in mind, the observed decay of $|g_1^0|$ has most often been attributed to the secular evolution of RFPs (Gubbins, 1987; Gubbins et al., 2006). In particular, various authors have stressed the importance of the evolution of the Southern Hemisphere RFPs underneath the southern tips of South America and Africa (Bloxham and Gubbins, 1985; Gubbins, 1987; Bloxham et al., 1989; Olson and Amit, 2006; Terra-Nova et al., 2016). For example, Olson and Amit (2006) and Finlay et al. (2016a) employed geomagnetic secular variation models to determine core flow at the CMB, and combined these flow and field models to map the associated contributions to axial dipole decay. Olson and Amit (2006) show that as much as roughly 80% of the instantaneous change in the axial dipole for 1980 may be the result of meridional advection of the field. Over archeomagnetic timescales (in particular the past 3 ka) Terra-Nova et al. (2015) found that RFPs have existed and that they contribute to axial dipole decay, this signal being clearer especially over the past several centuries when resolution of field models is greater. In particular, by using a null-flux line (where $B_r = 0$) as a magnetic equator in place of the geographic equator, they showed that spherical harmonic field components of degree 4 and higher are important in describing RFP evolution. They were able to partition the flux patches into a variety of types and quantified the contribution of each to the decay of $|g_1^0|$.

Models of Earth's internal field can generally be divided in two types: those that adopt the frozen-flux approximation (Roberts and Scott, 1965), that is they neglect diffusive contributions to secular variation (e.g. Bloxham and Gubbins, 1986; Constable et al., 1993; Lesur et al., 2010; Wardinski and Lesur, 2012); and those that do not (e.g. Jackson et al., 2000; Gillet et al., 2013, 2015; Finlay et al., 2016b). In frozen-flux models field evolution is rather restricted, there can be no net change in magnetic flux through a given RFP and RFPs are not allowed to merge or divide (Backus, 1968). This may be a problem as the intensification of reversed flux may well be the result of flux expulsion (Bloxham, 1986), a diffusive process that is absent from frozen-flux field models. Some models additionally conserve radial vorticity (e.g. Jackson et al., 2007; Asari and Lesur, 2011), so that poleward migration of RFPs is allowed only if there is an associated change in the morphology of that patch (Jackson, 1996). With such constraints, RFPs are then expected to contribute to axial dipole decay only by growing in surface area or by migrating towards the geographic poles. In what follows, we will therefore refrain from using frozen-flux models.

In this study, we build upon this previous work to address three objectives. Firstly, we evaluate the impact of the choice of the magnetic equator on RFP characteristics. As we will show later, the use of a magnetic equator with a relatively complex morphology can hamper the robust characterisation of reversed flux evolution, and a spatially smooth equator is therefore more appropriate for our analysis. The second objective is to quantify the importance of the reversed portion of the field for axial dipole decay, relative to the unreversed or normal part of the CMB field. Finally, we evaluate what characteristics of the RFP secular evolution contribute to this decay, specifically their intensification, migration, and growth in combined surface area.

This work is outlined as follows: section 2 specifies the field models used for our analysis, followed by our means of RFP identification in section 3. Sections 4 and 5 present respectively how the reversed and normal contributions to axial dipole decay are computed, and how this decay is interpreted in terms of RFP evolution. Our results are discussed in more detail in section 6 which also concludes our work.

2. Field models

We employed the field models gufm1 (Jackson et al., 2000), COV-OBS.x1 (Gillet et al., 2015), and CHAOS-6 (Finlay et al., 2016b) for the time periods 1840-1990, 1840-2015, and 1999-2015 respectively. The first model has been used in earlier works concerning reversed flux evolution (e.g. Gubbins et al., 2006, Olson and Amit, 2006, Terra-Nova et al., 2015) and the use of COV-OBS.x1 and CHAOS-6 allows us to extend their analysis by 25 years. Additionally, the lengths of the investigated periods for gufm1 and COV-OBS.x1 are larger than all non-dipole secular variation timescales (Lhuillier et al., 2011), such that significant temporal variation of the non-dipole field (and therefore that of reversed flux) is captured.

Among these field models there are similarities in terms of the data they are built upon. For example, the models gufm1 and COV-OBS.x1 rely on the compilation made by Jackson et al. (2000) (described in detail by Jonkers et al., 2003), which includes observations of marine and land surveys, observatory annual means (OAMs), and satellite data from the POGO and Magsat missions. Also, COV-OBS.x1 and CHAOS-6 both incorporate recent directional and intensity observations from the missions Ørsted, CHAMP, SAC-C, and Swarm, as well as OAMs up to the years 2013.5 and 2015 respectively. Moreover, the three models are constructed without the use of the frozen-flux approximation, so that the temporal evolution of RFPs is not further restricted.

The field models use different underlying modelling strategies, which result in different spatial and temporal behaviour, even at times when the same data are used. The models gufm1 and CHAOS-6 employ regularisation that ensures convergence of the spatial and temporal field spectra, while satisfactorily fitting the data. By contrast, COV-OBS.x1 is the result of a Bayesian (stochastic) inference obtained with *a priori* means and covariance information (for details see Gillet et al., 2013). This model comprises an ensemble of members, all of which fit the data satisfactorily and none of which are regularised. This ensemble enables us to determine uncertainties in field structure and derived quantities.

For all models we computed B_r for yearly intervals using a spherical harmonic expansion up to degree 14 on a 0.45°×0.45° latitude-longitude grid (i.e., 400×800 grid points). Several integral quantities (discussed in the following sections) were computed on the same grid for gufm1, the COV-OBS.x1 mean model, all 100 COV-OBS.x1 ensemble members, and CHAOS-6. The use of a higher resolution grid was tested (up to double the resolution) and did not yield significantly different results.

3. Identification of RFPs using a magnetic equator

3.1. Choice of magnetic equator

The first step in describing reversed flux is selecting a magnetic equator that partitions the CMB into two magnetic hemispheres (which may not be of equal surface area), each characterised by its dominant sign of radial flux. Reversed flux patches are then regions where the sign of B_r is opposite to the dominant sign of flux of the magnetic hemisphere in which they reside. The choice of the magnetic equator is non-unique; previous studies have employed both low (Olson and Amit, 2006) and high morphological complexity (Terra-Nova et al., 2015). It is sensible to define the magnetic equator according to a null-flux curve of a field truncated to a certain spherical harmonic degree $l_{\rm max}^{\rm eq}$. For example, truncating to the axial dipole component alone gives the geographic equator, a full degree 1 expansion yields a great circle tilted with respect to the geographic equator, and a higher degree multipole expansion yields an undulating curve. Note that a magnetic equator constructed using a degree of truncation $l_{\rm max}^{\rm eq} < 14$ will in general not align with null-flux curves of the degree 14 magnetic field used in this study.

3.2. Construction of a discrete magnetic equator

Any definition of the magnetic equator that depends on the morphology of the CMB field will evolve through time. Terra-Nova et al. (2015) presented and employed an algorithm that allows the determination of the magnetic equator for any given field morphology. Their algorithm finds an initial longitude along which there is only one location where $B_r = 0$ (strictly speaking where there is only one change in sign of B_r) and then repeatedly selects the closest grid location to this point at which $B_r = 0$ as the next point on the equator. Joining these grid points together then defines a discretised magnetic equator.

Our method of defining the magnetic equator is based on the algorithm of Terra-Nova et al. (2015), although we extended it in two ways. Firstly, it can not always be guaranteed that there exists an initial longitude along which there is only one location where $B_r = 0$. This can for example be the case when an RFP resides on the geographic North Pole. As an alternative approach, we chose an arbitrary initial longitude and selected the latitude at which $B_r = 0$ closest to the geographic equator. We do this by searching for a change in sign of B_r on our grid and then use a linear interpolation between grid points to find the location where $B_r = 0$. This location is then taken as the starting point of the discrete magnetic equator.

Secondly, we found that the magnetic equator constructed by the algorithm of Terra-Nova et al. (2015) was very sensitive to the structure of the magnetic field, particularly near the geographic equator when multiple null-flux curves were relatively close. There were cases where the iterative construction of the equator incorrectly joined nearby but separate null-flux curves, manifest by a local jump in the curvature of the magnetic equator. In order to enforce smoothness in the magnetic equator we scan along nearby lines of equal longitude for locations which have a change of sign in B_r, constructing a set of candidate locations defining the next point on our discrete magnetic equator. Then, we compute an unsuitability norm $\chi_i = \alpha s_i + \beta\zeta_i$ for every i^{th} candidate location, which involves both distance (s_i) and the change in tangential angle (ζ_i) between the current and candidate locations. The coefficients α and β describe the importance of distance and smoothness respectively. We fix the value of α and select β in a number of steps. Initially, we set $\beta = 0$ and select the candidate location that minimises χ_i (this mimics the algorithm of Terra-Nova et al. (2015)). If $\zeta_i > 3\pi/4$, we deem this point unacceptable and progressively increase β until the candidate point that minimises χ_i has an an associated $\zeta_i < 3\pi/4$. We then accept this candidate point as the next location on our discrete magnetic equator.

Having defined the magnetic equator we assign the dominant radial magnetic flux in the northern magnetic hemisphere to have negative sign and positive for the southern magnetic hemisphere. Within each magnetic hemisphere any grid point at which the sign of B_r is different from the dominant sign is assigned to be reversed. This defines the distribution of reversed flux in a point-wise manner.

3.3. Quantifying reversed flux

Any choice of magnetic equator presents problems for the identification of reversed flux. Using the geographic equator as the magnetic equator is undesirable as the Earth's dipole field is tilted; consideration of this component alone fragments individual low-latitude features into separate reversed and normal regions (Fig. 2a and 2b). This results in a substantial increase in the number of reversed flux regions which would otherwise not be considered as reversed. Conversely, an $l_{\max}^{\mathrm{eq}} = 14$ multipole expansion results in diversions of the equator to high latitudes encompassing large geographic areas. For example, for the year 1900 there is a large intrusion of the magnetic equator into the southern geographic hemisphere, caused by the connection of the reversed flux beneath the South Atlantic to the northern magnetic hemisphere (Fig. 2i and 2j). We assert that for the field models considered in this work this region should be considered a reversed flux patch in the southern magnetic hemisphere, because there are times when this region is present but is not connected to the northern magnetic hemisphere.

This effect is quantified in Figure 3a where we show the combined reversed flux area A_R (see section 5 for details) normalised by the total CMB area S as a function of time, using a magnetic equator obtained with $l_{\max}^{\mathrm{eq}} = 14$. There are clear discontinuities in A_R which occur when null-flux curves defining the boundaries of reversed flux disconnect from or connect to the magnetic equator. Of further note is that the spread among the COV-OBS.x1 ensemble members is relatively large near the end of the 20$^{\mathrm{th}}$ century, precisely when data quality and quantity is relatively high. The change in ensemble spread during this period reflects how for this type of magnetic equator the identification of reversed flux is particularly sensitive to small-scale features of the field. For example, a very small temporal change in the morphology of the field may yield the merging of a RFP and the opposing magnetic hemisphere, which will strongly affect the secular variation of A_R. On the other hand, similar change in field structure elsewhere that does not result in such a merge, will have little effect on A_R. Therefore, the use of a magnetic equator defined with $l_{\max}^{\mathrm{eq}} = 14$ makes it difficult to robustly quantify the temporal evolution of reversed flux, and we therefore deem it unacceptable for our analysis. Of additional interest in this figure is that although the results for COV-OBS.x1 and CHAOS-6 appear to be consistent, there is an apparent disagreement between COV-OBS.x1 and gufm1 during the first four decades of the time period shown: A_R according to gufm1 shows an almost constant value, whilst A_R according to COV-OBS.x1 exhibits rapid decline. This time period coincides with the start-up period for the COV-OBS.x1 model, and is likely to be a manifestation of an end effect (N. Gillet, personal communication, 2016). For this reason, we focus attention on the period 1880-2015 for the remainder of this work.

A magnetic equator that is defined using a low degree of truncation will limit the occurrence of large intrusions, whereas increasing $l_{\max}^{\mathrm{eq}}$ reduces the combined surface area of divided low-latitude reversed flux. Figures 2c to 2h show the effect of the choosing of $l_{\max}^{\mathrm{eq}} \in \{1, 3, 4\}$ on the identification of reversed flux. The choice of $l_{\max}^{\mathrm{eq}} = 1$ is undesirable as it still fragments low-latitude features particularly underneath the Pacific. Conversely, for $l_{\max}^{\mathrm{eq}} = 4$ the equator assumes a shape that resembles the hemispherical intrusion of $l_{\max}^{\mathrm{eq}} = 14$. The choice $l_{\max}^{\mathrm{eq}} = 3$ gives the most structured magnetic equator, such that the combined surface area of divided low-latitude reversed flux is acceptable, while avoiding the problematic intrusion.

The sensitivity of reversed flux identification to magnetic equator complexity has also been quantified by computing time series of A_R/S for various $l_{\max}^{\mathrm{eq}}$ (Fig. 4). It appears that decreasing $l_{\max}^{\mathrm{eq}}$ generally yields a larger value of A_R/S, due to the associated inclusion of divided low-latitude RFPs. However, the trends among all continuous curves remain similar. It is also of note that the apparent lowest degree of complexity for the magnetic equator we can employ before any discontinuities develop is $l_{\max}^{\mathrm{eq}} = 4$. Nevertheless, this is not a robust choice for the magnetic equator, as it still yields jumps in magnetic equator morphology. These jumps can not be detected from the A_R time series (Fig. 4); however, they can be seen in other quantities. For example, the change in magnetic equator morphology between 1946 and 1947 yields negligible overall change in A_R (Fig. 5), whereas the classification of B_r within the magnetic hemispheres has changed abruptly. Also, these maps illustrate the unrealistic identification of normal flux, with normal features in the Southern Hemisphere completely detached from the Northern Hemisphere. Considering these difficulties with $l_{\max}^{\mathrm{eq}} = 4$, we instead adopt $l_{\max}^{\mathrm{eq}} = 3$ for the remainder of this work, and to maintain consistency among our results we do so for all field models. Under this definition of the magnetic equator, for the COV-OBS.x1 model Fig. 3b shows an initial fall in the total flux patch area, a stable period between 1880 and 1920 when A_R/S is constant, and a gradual increase in A_R/S to the present day. This behaviour is largely parallelled by gufm1, although it has no initial decay and for all times A_R/S is less than that calculated from COV-OBS.x1. Moreover, we again find agreement among CHAOS-6 and COV-OBS.x1 results, although the former model appears to yield a slightly lower rate of change in A_R/S. Lastly, Fig. 3b shows that over the time periods investigated RFPs do not cover more than 20% of the CMB.

An alternative characterisation of RFPs, in addition to their area, is by their typical spherical harmonic degrees. For our choice of magnetic equator $l^{\mathrm{eq}}_{\mathrm{max}} = 3$, figure 6a shows the effect of truncating the field to degree l_{max} by its flux patch area A_R/S as a function of time. There appears to exist a minimum degree of truncation required to resolve RFPs, which is time-dependent. For example, during the second half of the investigated period there are almost no RFPs for $l_{\mathrm{max}} \leq 3$; however, setting $l_{\mathrm{max}} = 4$ yields a marked increase in RFP area. In earlier times, setting $l_{\mathrm{max}} = 4$ resolves relatively less reversed flux and it appears that $l_{\mathrm{max}} = 5$ is required to resolve the majority of RFPs for that period. Also, Fig. 6a shows that l_{max} and A_R are not strictly positively correlated, as A_R/S exhibits a decline within the ranges $l_{\mathrm{max}} = 9$ to 11 and $l_{\mathrm{max}} = 5$ to 8 for the approximate periods 1880-1910 and 1950-2015, respectively.

To assess the robustness of the above characterisation of reversed flux we briefly consider the effect of applying the same analysis using a magnetic equator defined using $l^{\mathrm{eq}}_{\mathrm{max}} = 14$. Figure 6b shows two key features: first is the signature of the intrusion which is particularly noticeable between 1880 and 1920 for $l_{\mathrm{max}} \geq 10$. Second is that we find a clearer signature of the characteristic spherical harmonic degree defining RFPs of least 5. This matches the results presented in Fig. 6a as in both cases an l_{max} of at least 5 is required to resolve a significant portion of the reversed field. Lastly, Figure 7 shows the total flux patch area for $l_{\mathrm{max}}^{\mathrm{eq}} = 3$ and as a function of l_{max} when time averaged. It shows for gufm1 and the COV-OBS.x1 mean model that there is no single characteristic minimum degree for the whole of the period and that the inclusion of degrees 4 and 5 yields the greatest increases in A_R/S. This illustrates the particular importance of these degrees for resolving reversed flux over the corresponding time periods. However, the CHAOS-6 results demonstrate that for approximately the past two decades that RFPs are predominantly degree 4 features, and that there is also a small contribution from degree 3, reflecting a change in the typical wavelength of these features.

4. Contributions to the axial dipole

Having defined RFPs we are now in a position to compute the contributions from the combined area of RFPs, S_R, and the combined area of normal field (i.e. the remaining regions), S_N, to the axial dipole coefficient g_1^0. Following Eq. (1) we can partition these contributions as follows

$$\begin{aligned} g_1^0(t) &= \frac{3c}{8\pi a^3}\Big(\int_{S_R(t)} B_r(\mathbf{r},t)\cos\theta\,\mathrm{d}S + \int_{S_N(t)} B_r(\mathbf{r},t)\cos\theta\,\mathrm{d}S\Big) \\ &= g_{1,R}^0(t) + g_{1,N}^0(t) \end{aligned} \tag{2}$$

The above expression explictly shows how g_1^0 may be expressed in terms of the reversed and normal flux distribution. Using the grid specified in section 2, $g_{1,R}^0$ and $g_{1,N}^0$ are computed through 2-D trapezoidal integration at yearly intervals, where only quadrilaterals with four nodal points that are designated reversed contribute to $g_{1,R}^0$, while the remaining quadrilaterals contribute to $g_{1,N}^0$.

The time-dependence of the contributions $g_{1,R}^0$ and $g_{1,N}^0$ is shown in Fig. 8a and 8b, respectively. Both gufm1 and the ensemble mean of COV-OBS.x1 show a monotonic increase in $g_{1,R}^0$ from about 1900 onwards. According to either model, the increase in $g_{1,R}^0$ over the 20$^{\text{th}}$ century amounts to approximately $1.3 \cdot 10^3$ nT: this is roughly two-thirds of the decay in $|g_1^0|$ (of about $1.8 \cdot 10^3$ nT, see Fig. 1) over that time. However, it should be noted that our estimate of the reversed axial dipole contribution is likely to be a lower bound due to differences in the magnetic equator we consider and the geographic equator which defines the axial dipole. For example, by employing our magnetic equator there exist field features that are considered reversed and still enforce the actual dipole.

Figure 8b shows the time dependence of $g^0_{1,N}$, which is an important but a less frequently considered contribution to the axial dipole. Its increase since 1900 parallels that of $g^0_{1,R}$, although to a lesser extent. Indeed, the change in $g^0_{1,N}$ is one third of the decay in $|g^0_1|$ over the 20$^{\mathrm{th}}$ century. Comparing figures 3b and 8a we see that, compared with COV-OBS.x1, gufm1 provides a lower value for A_R and its corresponding $g^0_{1,R}$.

5. Characterisation of reversed flux patch evolution

In this section we focus on characterising the increases in $g^0_{1,R}$ and $g^0_{1,N}$ over the 20th century in terms of reversed- and normal-flux evolution respectively, which have jointly contributed to the decline of $|g^0_1|$ over this period. Inspection of Eq. (2) shows that secular increases in $g^0_{1,R/N}$ can be due to a change in one or more of $S_{R/N}$ (growth/reduction of combined area), the latitude-weighted area (poleward/equatorward migration), or B_r (flux (de)intensification). We test which of these effects have importance for the evolution of $g^0_{1,R/N}$ by computing the quantities:

$$
\begin{aligned}
A_R(t) &= \int_{S_R(t)} \mathrm{d}S\ , && (3)\\
\Phi_{R/N}(t) &= \frac{1}{A_{R/N}(t)} \int_{S_{R/N}(t)} |B_r(\mathbf{r}, t)|\, \mathrm{d}S\ , && (4)\\
\Theta_{R/N}(t) &= \frac{1}{A_{R/N}(t)} \int_{S_{R/N}(t)} |\cos\theta|\, \mathrm{d}S\ , && (5)
\end{aligned}
$$

which represent, respectively, the combined reversed surface area (note that $A_N(t) + A_R(t) = S$), the average unsigned B_r over $S_{R/N}$, and the average unsigned cosine latitude weighting factor average over $S_{R/N}$.

The time-dependency of A_R has already been shown in Fig. 3b. As mentioned above it shows a gradual growth over the 20th century which amounts to a relative increase of about 11% for the COV-OBS.x1 ensemble average and more than 30% for gufm1. The correlation between these increases and those in $g^0_{1,R}$ (Fig. 8a) suggests that the decay in $|g^0_1|$ may be linked to an increase in RFP area. However, this takes no account of where RFPs are located. Figure 9a shows that Θ_R has increased by 27% according to COV-OBS.x1 and 51% according to gufm1 over the 20th century. This indicates that in these models RFPs show a significant average poleward migration. Of further note is that since 2000, Θ_R has been approximately constant and therefore has not contributed itself to any recent change in g_1^0, in contrast to its significant role over the past century. Lastly, Fig. 9b shows that the average radial flux through RFPs has increased significantly over the 20th century by approximately 14% and 21% for COV-OBS.x1 and gufm1, respectively. In common with previous figures, the estimates for Φ_R from gufm1 are lower than those from COV-OBS.x1.

Taken together, the relative increases of A_R, Θ_R and Φ_R suggest that the decay in $|g_1^0|$ over the past century is manifest at the CMB as a combination of growth of RFP area, poleward migration, and flux intensification within RFPs over that period. Comparing the magnitudes of the increases in the quantities we consider, the relative increase in Θ_R is roughly twice that of A_R and Φ_R, such that more than half of the increase in $g_{1,R}^0$ over the 20th century may be attributed to poleward migration and the remaining increase may be equally ascribed to each of reversed flux expansion and intensification (Table 1).

The evolution of the normal field is characterised by the time-series of the quantities Θ_N and Φ_N, shown in Fig. 10a and 10b, respectively. It is clear that Θ_N has remained relatively constant over the 20th century with a relative change of less than 5% over this period for both COV-OBS.x1 and gufm1. The average intensity of normal-flux, Φ_N, has undergone a relative increase of approximately 10% over the investigated period, a change that strengthens the axial dipole. The overall influence of the changes in the normal-field quantities is to weaken the axial dipole, mainly due to the change in A_N, with the impact of changes in Θ_N and Φ_N on g_1^0 approximately cancelling (Table 1).

6. Discussion and conclusions

We set out to address three issues in the determination of RFP evolution and their influence on the decay of the axial dipole. First, we needed to define a magnetic equator enabling the identification of RFPs. We investigated the use of null-flux curves for different degrees of truncation of the magnetic field. We found that the use of a degree three field provided a robust method of identifying RFPs, and that RFPs are features of at least degree 5. Our choice of magnetic equator contrasts with that of Terra-Nova et al. (2015) who used a null-flux curve of the total field (in this case of degree 10) as the magnetic equator, and with Olson and Amit (2006) who used the geographic equator. As we show, neither of these are effective for our time period: setting $l_{\text{max}}^{\text{eq}}$ to be l_{max} of the total field produces a large intrusion of the magnetic equator into the southern hemisphere during approximately 1880-1920, while the use of a geographic equator fragments low-latitude features. Over a longer archeomagnetic timescale (about the past three millennia), Terra-Nova et al. (2015) showed that RFPs are features of degree at least 4, which is consistent with our results.

The second issue we addressed was to quantify the contribution of the reversed and normal flux regions on the CMB to the decay of the axial dipole. The g_1^0 coefficient can be altered by changes in the area of reversed or normal flux (A_R and A_N), the latitudinal migration of flux patches (as characterised by Θ_R and Θ_N), or changes in flux intensity within the patches (as characterised by Φ_R and Φ_N); first-order estimates of each of these effects are given in Table 1. We found that roughly two-thirds of the decay over the 20$^{\text{th}}$ century may be attributed to RFPs and one-third to the evolution of the normal field. Although normal field provides a smaller contribution, it is sufficiently significant such that the decay of the axial dipole can not exclusively be attributed to the reversed part of the field (Gubbins, 1987). However, given that the total reversed surface area relative to the area of the CMB is 20% at most, the axial dipole appears to be particularly sensitive to changes in the reversed portion of the field compared to the normal field.

Third, we find that in the field models considered, the most important contributions to the decrease in $|g_1^0|$ arise from the changed partitioning of reverse and normal field area at the CMB, and the poleward migration of RFPs. It is interesting to note that these dominant contributions over the past century may not continue to reflect the current (or future) secular variation of the axial dipole. For example, the contribution to dipole decay arising from the average poleward migration of RFPs plateaued at around epoch 2000 (Fig. 9a); the continuing decrease of g_1^0 since that time is primarily due to increases in the average amplitude of reversed flux within the RFPs (Fig. 9b).

Our results are consistent with the work of Terra-Nova et al. (2015) who find a similar time dependence over the 20th century for the contribution of the reversed field to the axial dipole, although this is to be expected as they employ the CALS3k.4b field model which is constrained by gufm1 for the years 1840 to 1990 (Korte and Constable, 2011). Additionally, by using gufm1 for the same period as in this study, Olson and Amit (2006) find that the fall in $|g_1^0|$ is mostly due to secular variation in the Southern Hemisphere. This is again consistent with our results as we find that the evolution of RFPs, which reside predominantly in the Southern Hemisphere, account for most of the $|g_1^0|$ decay. Our results also demonstrate the significance of poleward migration of RFPs for axial dipole decay, similar to the studies of Olson and Amit (2006) and Finlay et al. (2016a). However, both studies highlight the importance of equatorward flow of intense normal flux beneath the southern Indian Ocean, which contrasts with our finding that the reversed flux contribution to axial dipole decay is more than twice as large as its normal counterpart. We find evidence for equatorward advection of normal field, but its contribution to axial dipole decay appears to be relatively small. It is possible that these discrepancies can be explained by the fact that the flow models from the previous studies are constrained by the frozen-flux approximation, unlike our approach.

In this study we compared results from COV-OBS.x1 and gufm1; although based on similar data the models show a marked difference in the RFP identification from 1840 to 1880. The major difference during this period is in the representation of small scale magnetic features. Whereas gufm1 has relatively strong temporal and spatial damping that penalises small scales, by contrast COV-OBS.x1 has no damping, and apparently has anomalously strong small scale features between 1840 and 1880 that is likely due to an end effect (N. Gillet, personal communication, 2016). For this reason we restrict attention to the period of 1880 onwards. As the investigated quantities (Eq. 2-5) are particularly sensitive to the distribution and intensity of the short-wavelength reversed field, the relatively strong regularisation inherent in gufm1 has a signature in all of our plots that characterise the area and magnitude of RFPs, by having markedly lower estimates of our descriptive quantities than COV-OBS.x1 (Fig. 3, 8a and 9). Despite these differences, the general trends agree and therefore both models support the conclusions that we have reached.

Both gufm1 and COV-OBS.x1 are constructed without frozen-flux constraints on RFP evolution. The use of models that employ such constraints (e.g. Bloxham and Gubbins, 1986; Constable et al., 1993; Lesur et al., 2010; Wardinski and

Lesur, 2012) may yield significantly different results than those presented in this work. This is especially the case for the quantities A_R and Φ_R that respectively represent RFP surface area and intensity. If models that additionally conserve radial vorticity were to be applied in our analysis (e.g. Jackson et al., 2007; Asari and Lesur, 2011), then this may also yield different results for the evolution of Θ_R, as in that case poleward migration of an RFP is allowed only if there is an associated change in the morphology of that patch (Jackson, 1996). Thus, for these models the decay of the axial dipole remains to be explained and further work will be required to determine how it may be attributed to different aspects of CMB field evolution. Within the models we have analysed, poleward migration of RFPs is an important contributor to 20^{th} century dipole decay; however, this process contributes little to the ongoing decay afther the year 2000.

7. Acknowledgements

We thank Vincent Lesur and Hagay Amit for reviewing our work and their constructive criticism. Additionally, we are grateful to Nicolas Gillet, Chris Finlay and Ciaran Beggan for their useful comments, which further improved this work. Lastly, we thank the National Space Institute of the Technical University of Denmark for their open-access repository of magnetic field models. M. C. Metman is supported by a studentship awarded as part of the Leeds-York NERC Doctoral Training Partnership (NE/L002574/1) and by the BGS University Funding Initiative PhD studentship (S305).

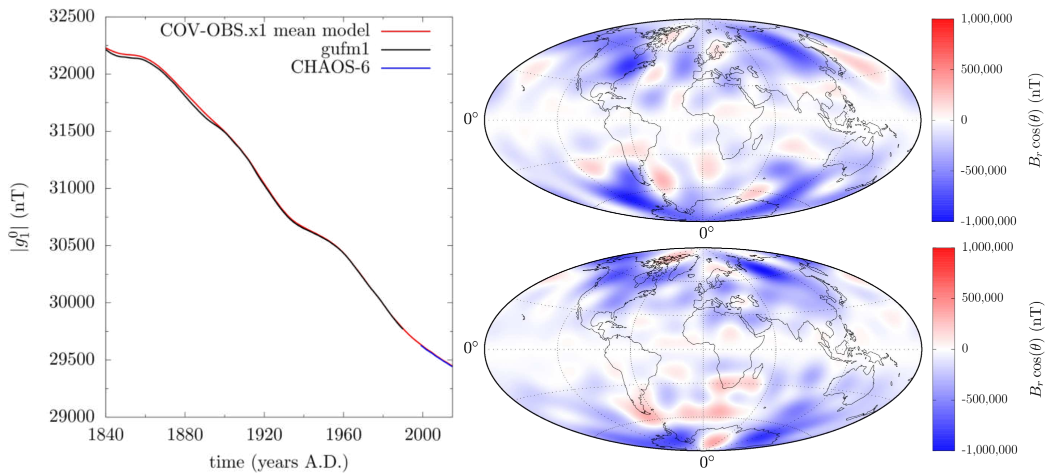

Figure 1: The magnitude of the axial dipole coefficient g_1^0 for the period 1840.0 to 2015.0 (left), and the spatial distribution of $B_r \cos(\theta)$ on the CMB for the COV-OBS.x1 mean model at epochs 1840.0 (top right) and 2015.0 (bottom right).

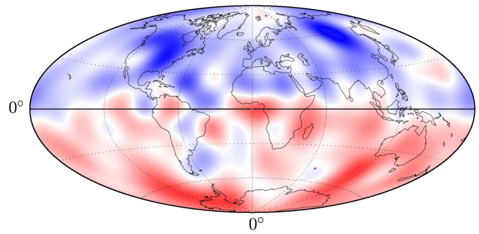
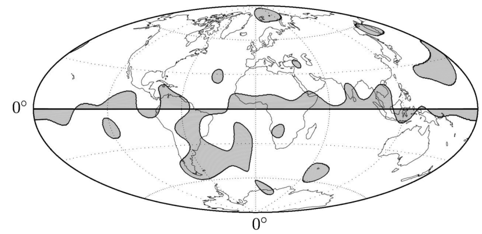

(a) B_r, geographic equator | (b) RFPs, geographic equator

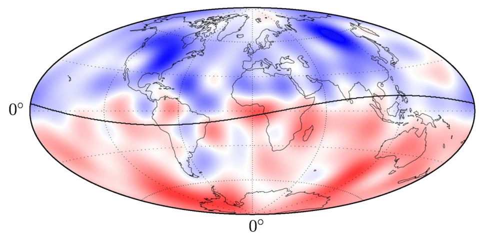
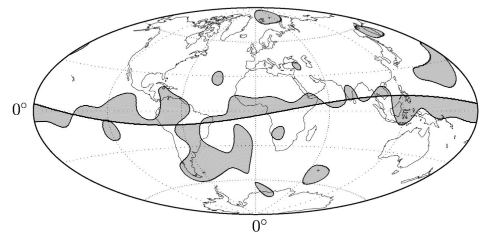

(c) B_r, $l_{\text{max}}^{\text{eq}} = 1$ | (d) RFPs, $l_{\text{max}}^{\text{eq}} = 1$

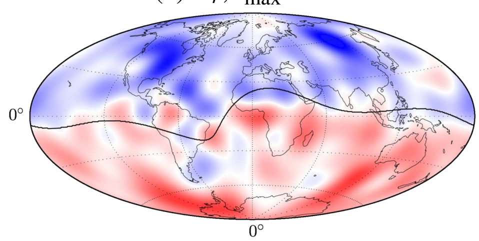
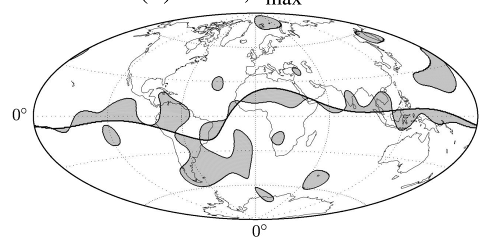

(e) B_r, $l_{\text{max}}^{\text{eq}} = 3$ | (f) RFPs, $l_{\text{max}}^{\text{eq}} = 3$

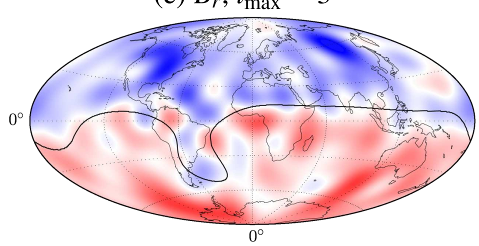
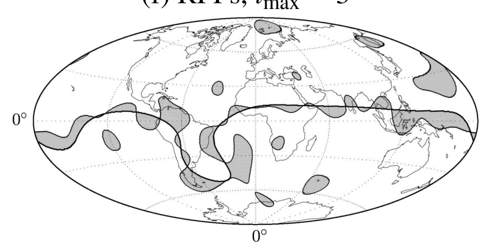

(g) B_r, $l_{\text{max}}^{\text{eq}} = 4$ | (h) RFPs, $l_{\text{max}}^{\text{eq}} = 4$

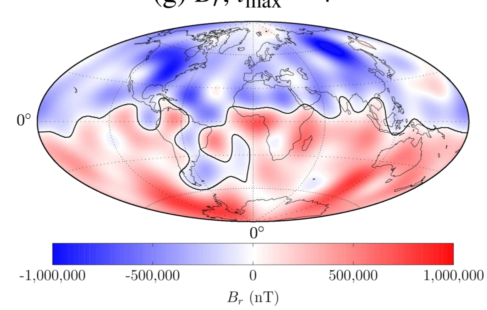

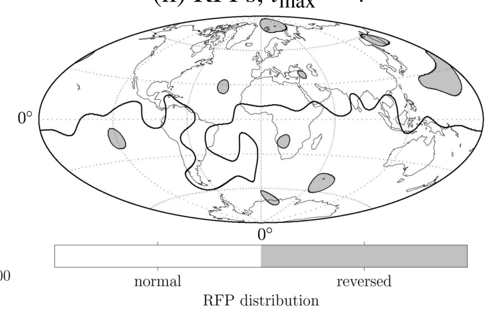

(i) B_r, $l_{\text{max}}^{\text{eq}} = 14$ | (j) RFPs, $l_{\text{max}}^{\text{eq}} = 14$

Figure 2: The radial field B_r on the CMB (left) and the associated distribution of RFPs (right) for epoch 1900.0 and several configurations of the magnetic equator (solid black line).

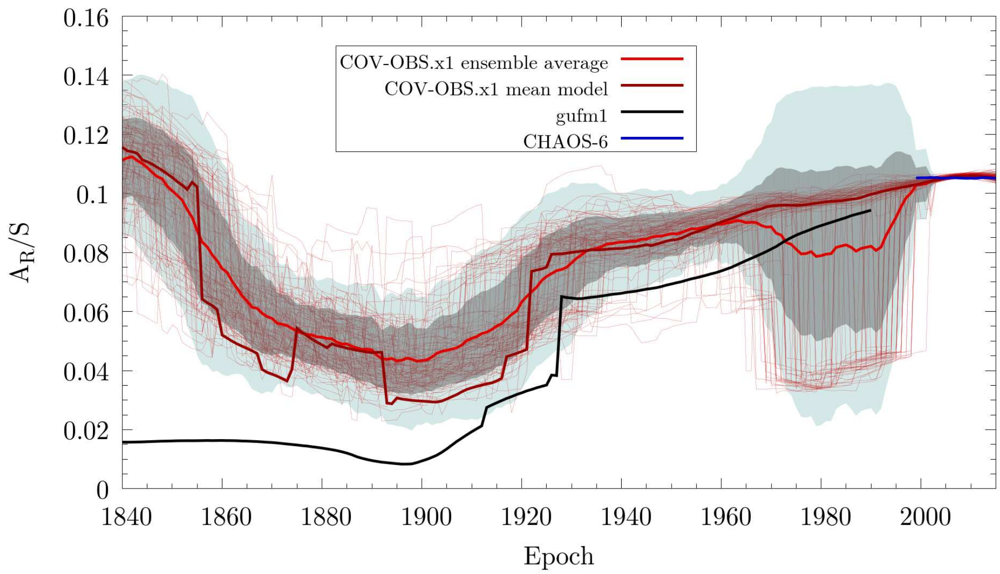

(a) $l_{\max}^{\text{eq}} = 14$

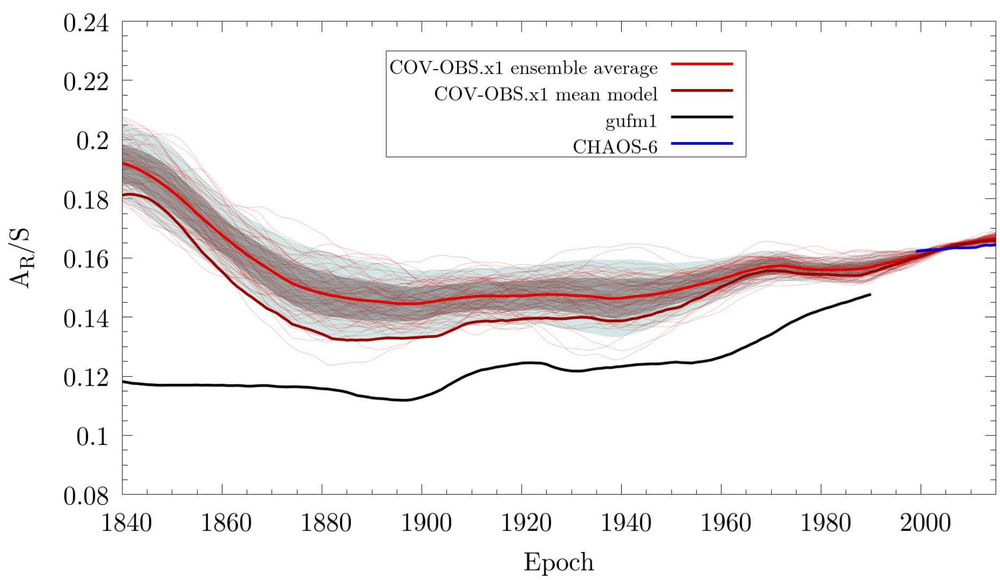

(b) $l_{\max}^{\text{eq}} = 3$

Figure 3: The combined reversed to CMB surface area ratio A_R/S as a function of time for all COV-OBS.x1 ensemble members, using a magnetic equator with $l_{\max}^{\text{eq}} = 14$ (a) and $l_{\max}^{\text{eq}} = 3$ (b). Shown are the results for gufm1 (black curve), the COV-OBS.x1 mean model (dark red curve), and all COV-OBS.x1 ensemble members (thin red curves). The thick light red curve is the average among the results for the ensemble members, and the dark and light gray areas correspond to confidence intervals of one and two times the standard deviation, respectively.

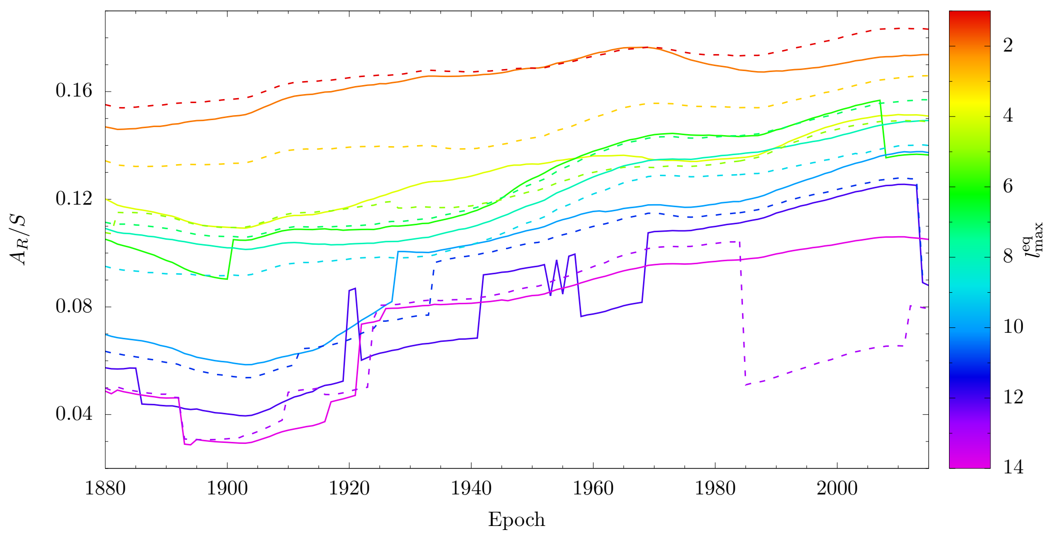

Figure 4: The combined reversed to CMB surface area ratio A_R/S as a function of time and for various $l_{\max}^{\rm eq}$. Solid and dashed curves represent even and uneven $l_{\max}^{\rm eq}$ respectively.

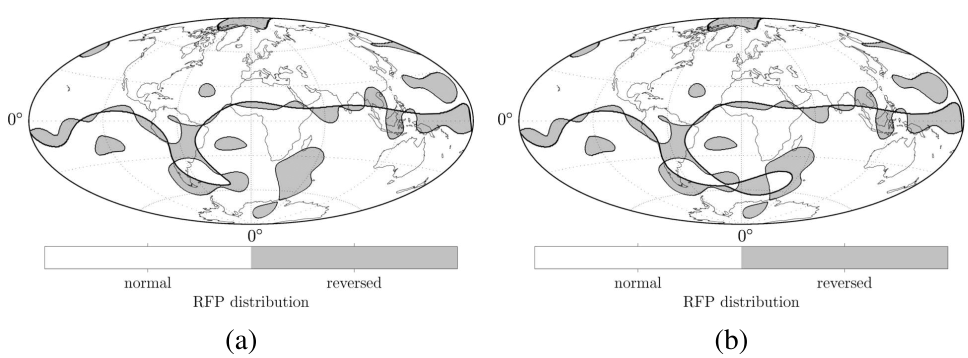

Figure 5: The distribution of reversed flux for epochs 1946.0 (a) and 1947.0 (b).

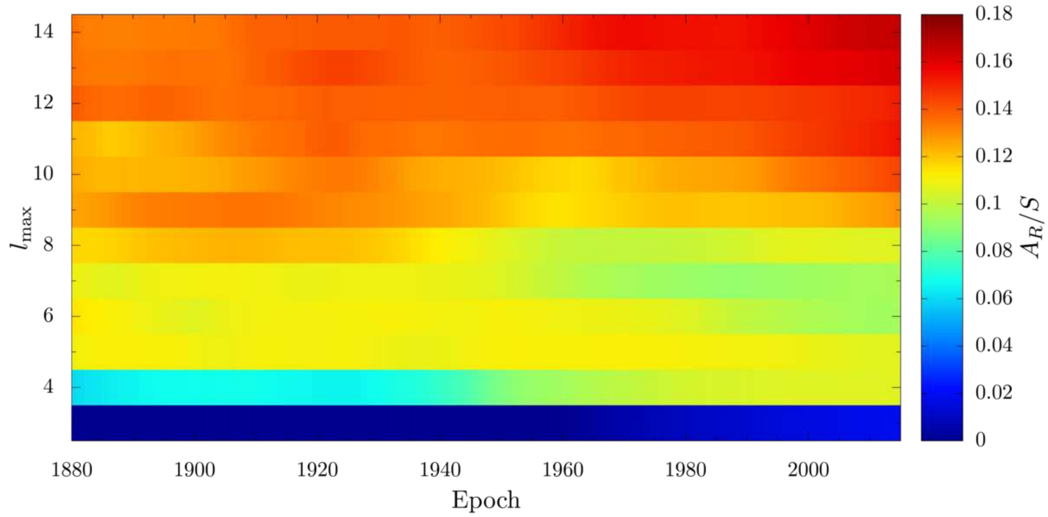

(a) $l_{\max}^{\mathrm{eq}} = 3$

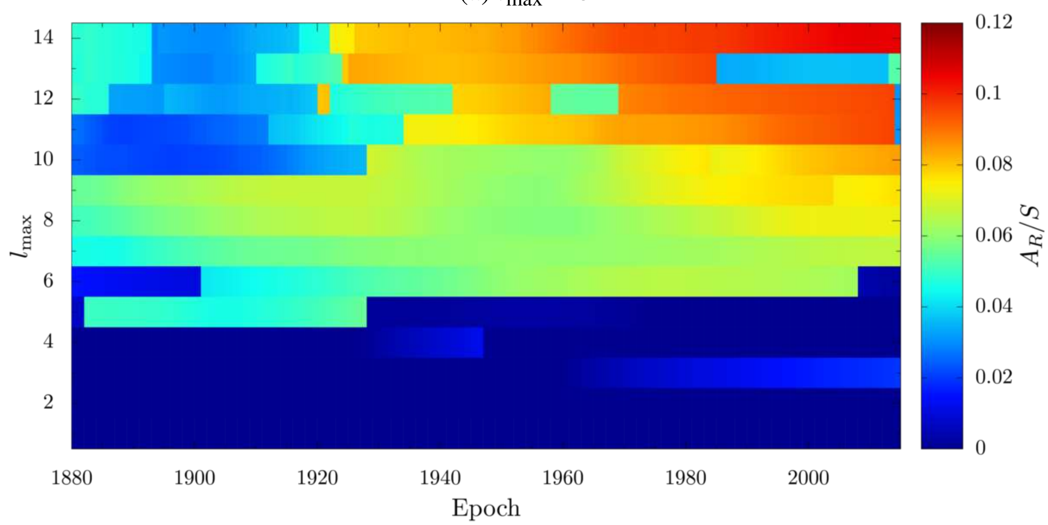

(b) $l_{\max}^{\mathrm{eq}} = 14$

Figure 6: The ratio of the combined RFP area relative to the CMB surface area A_R/S as a function of time and degree of truncation $l_{\max}$ for the COV-OBS.x1 mean model, using either a magnetic equator obtained with $l_{\max}^{\mathrm{eq}} = 3$ (a) or $l_{\max}^{\mathrm{eq}} = 14$ (b).

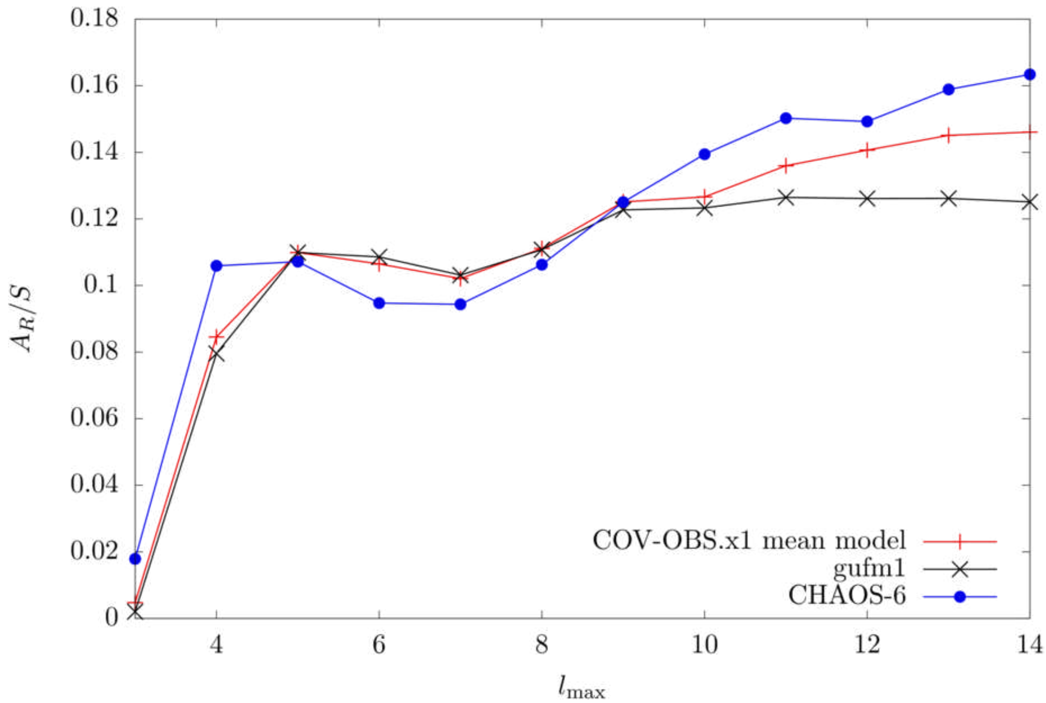

Figure 7: The ratio of the combined reversed flux area relative to the CMB surface area A_R/S averaged over the investigated periods with $l_{\max}^{\mathrm{eq}} = 3$ and as a function of $l_{\max}$.

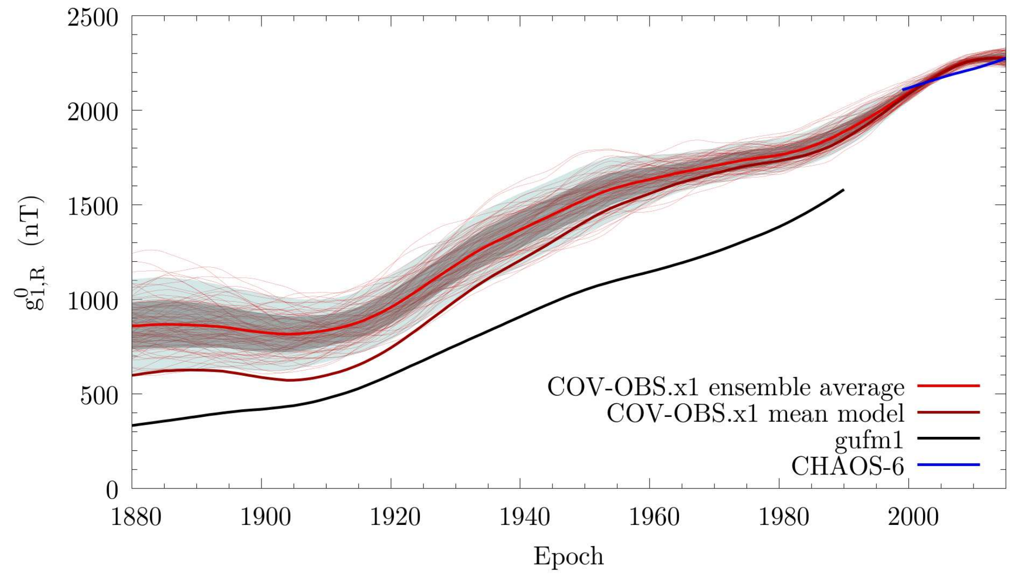

(a)

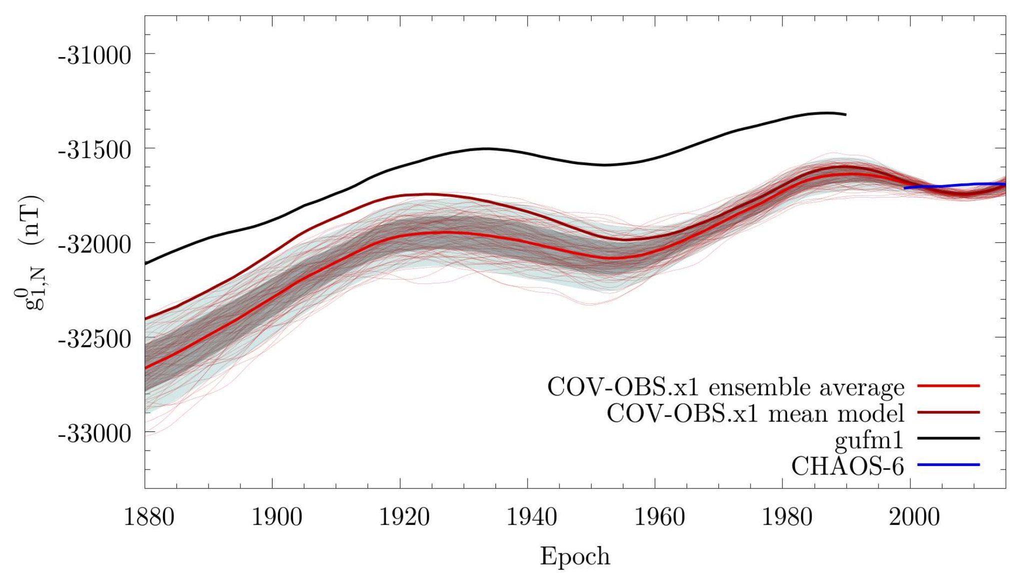

(b)

Figure 8: The reversed (a) and normal contributions (b) to the axial dipole field over the investigated periods (the same colouring as in Fig. 3 applies).

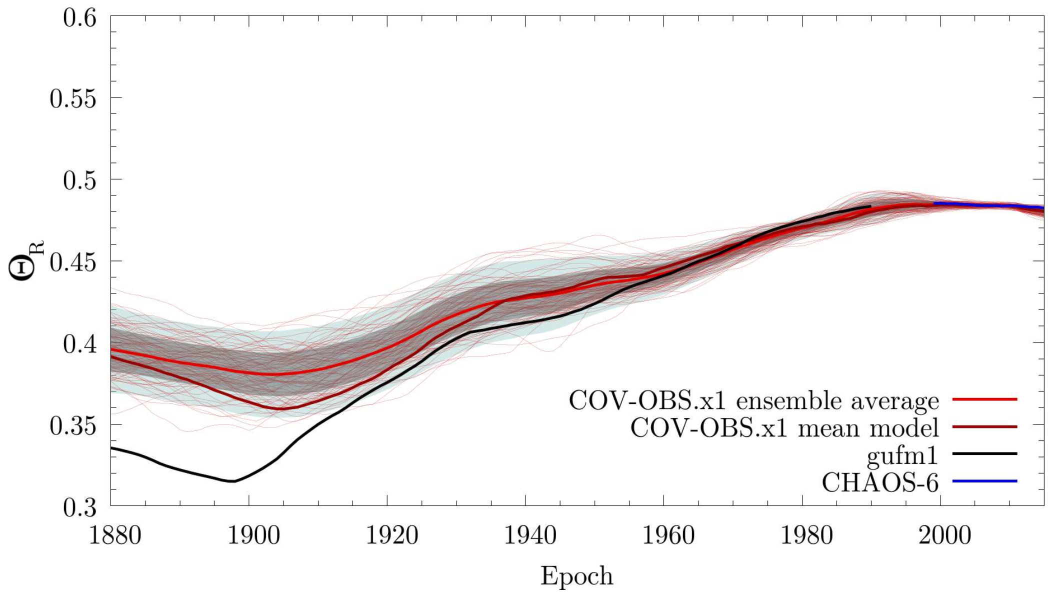

(a)

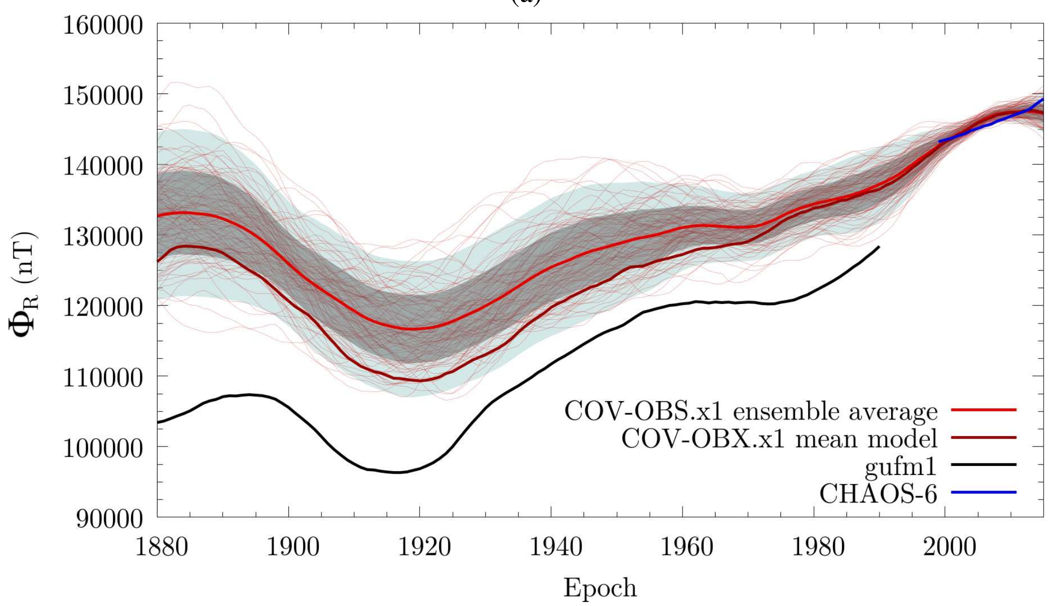

(b)

Figure 9: The average over the combined RFP area of $|\cos\theta|$ (a) and $|B_r|$ (b) as a function of time (the same colouring as in Fig. 3 applies).

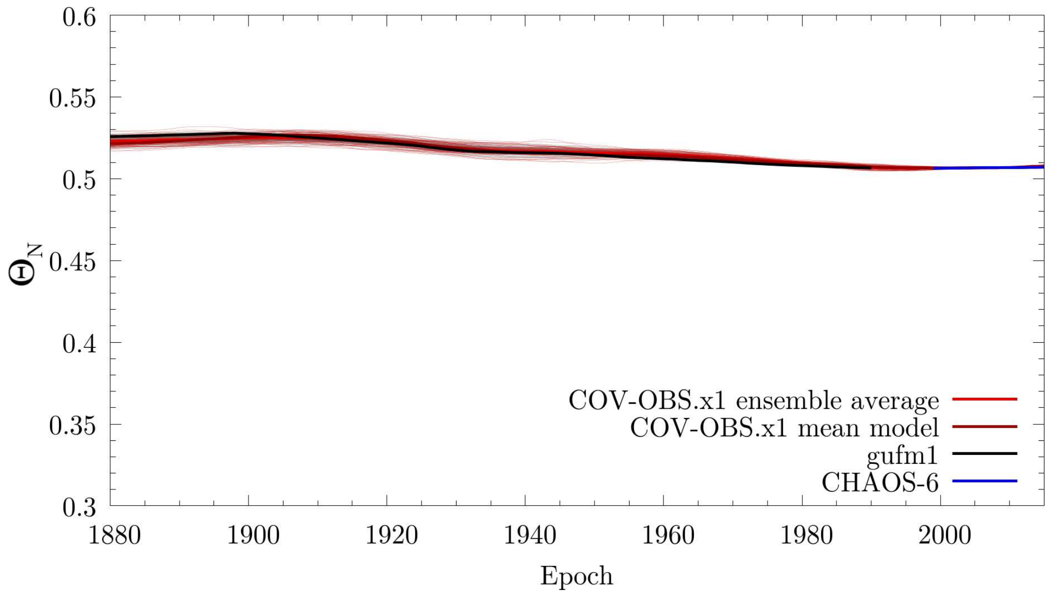

(a)

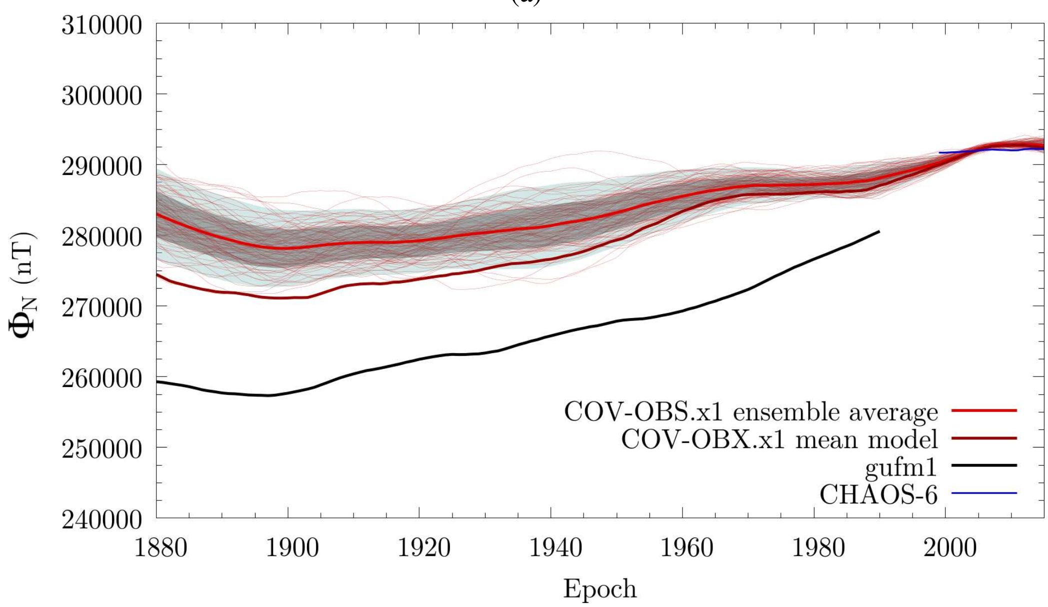

(b)

Figure 10: The average over the combined normal area of $|\cos\theta|$ (a) and $|B_r|$ (b) as a function of time (the same colouring as in Fig. 3 applies).

	A	Θ	Φ	total
$g^0_{1,R}$	0.3	0.7	0.3	1.3
$g^0_{1,N}$	0.6	0.2	-0.3	0.5

Table 1: The approximate impact of changes in the integral quantities A, Θ and Φ over the 20$^{\text{th}}$ century on the axial dipole contributions $g^0_{1,R/N}$ in units of 10^3 nT.

References

Asari, S. and Lesur, V. (2011). Radial vorticity constraint in core flow modeling. Journal of Geophysical Research: Solid Earth, 116(11).

Backus, G., Parker, R., and Constable, C. (1996). Foundations of Geomagnetism. Cambridge University Press, Cambridge.

Backus, G. E. (1968). Kinematics of geomagnetic secular variation in a perfectly conducting core. Philosophical Transactions of the Royal Society of London A: Mathematical, Physical and Engineering Sciences, 263(1141):239–266.

Barraclough, D. R. (1974). Spherical harmonic analyses of the geomagnetic field for eight epochs between 1600 and 1910. Geophysical Journal of the Royal Astronomical Society, 36(3):497–513.

Bloxham, J. (1986). The expulsion of magnetic flux from the Earth's core. Geophysical Journal International, 87(2):669–678.

Bloxham, J. and Gubbins, D. (1985). The secular variation of Earth's magnetic field. Nature, 317:777–781.

Bloxham, J. and Gubbins, D. (1986). Geomagnetic field analysis − IV. Testing the frozen-flux hypothesis. Geophysical Journal of the Royal Astronomical Society, 84(1):139–152.

Bloxham, J., Gubbins, D., and Jackson, A. (1989). Geomagnetic secular variation. Philosophical Transactions of the Royal Society of London, 329:415–502.

Constable, C. G., Parker, R. L., and Stark, P. B. (1993). Geomagnetic field models incorporating frozen-flux constraints. Geophysical Journal International, 113:419–433.

Finlay, C. C., Aubert, J., and Gillet, N. (2016a). Gyre-driven decay of the Earth's magnetic dipole. Nature Communcations, 7(10422).

Finlay, C. C., Olsen, N., Kotsiaros, S., Gillet, N., and Tøffner-Clausen, L. (2016b). Recent geomagnetic secular variation from Swarm and ground observatories as estimated in the CHAOS-6 geomagnetic field model. Earth, Planets and Space, 68(1):112.

Gillet, N., Barrois, O., and Finlay, C. (2015). Stochastic forecasting of the geomagnetic field from the COV-OBS.x1 geomagnetic field model, and candidate models for IGRF-12 International Geomagnetic Reference Field - The Twelfth generation. Earth, Planets and Space, 67(1).

Gillet, N., Jault, D., Finlay, C. C., and Olsen, N. (2013). Stochastic modeling of the Earth's magnetic field: Inversion for covariances over the observatory era. Geochemistry, Geophysics, Geosystems, 14(4):766–786.

Gubbins, D. (1987). A mechanism for geomagnetic polarity reversals. Nature, 326:167–169.

Gubbins, D., Jones, A. L., and Finlay, C. C. (2006). Fall in Earth's magnetic field is erratic. Science, 312:900–902.

Jackson, A. (1996). Kelvin's theorem applied to the Earth's core. Proceedings of the Royal Society of London A: Mathematical, Physical and Engineering Sciences, 452(1953):2195–2201.

Jackson, A., Constable, C., Walker, M., and Parker, R. (2007). Models of Earth's main magnetic field incorporating flux and radial vorticity constraints. Geophysical Journal International, 171(1):133–144.

Jackson, A., Jonkers, A. R. T., and Walker, M. R. (2000). Four centuries of geomagnetic secular variation from historical records. Philosophical Transactions of the Royal Society of London, 358:957–990.

Jonkers, A. R. T., Jackson, A., and Murray, A. (2003). Four centuries of geomagnetic data from historical records. Reviews of Geophysics, 41(2).

Korte, M. and Constable, C. (2011). Improving geomagnetic field reconstructions for 0-3 ka. Physics of the Earth and Planetary Interiors, 188(34):247 – 259.

Lesur, V., Wardinski, I., Asari, S., Minchev, B., and Mandea, M. (2010). Modelling the Earth's core magnetic field under flow constraints. Earth, Planets and Space, 62(6):503–516.

Lhuillier, F., Fournier, A., Hulot, G., and Aubert, J. (2011). The geomagnetic secular-variation timescale in observations and numerical dynamo models. Geophysical Research Letters, 38(9).

Olson, P. and Amit, H. (2006). Changes in Earth's dipole. Naturwissenschaften, 93(11):519–542.

Roberts, P. H. and Scott, S. (1965). On Analysis of the Secular Variation. 1. A Hydromagnetic Constraint: Theory. Journal of Geomagnetism and Geoelectricity, 17(2):137–151.

Terra-Nova, F., Amit, H., Hartmann, G. A., and Trindade, R. I. (2016). Using archaeomagnetic field models to constrain the physics of the core: robustness and preferred locations of reversed flux patches. Geophysical Journal International, 206(3):1890–1913.

Terra-Nova, F., Amit, H., Hartmann, G. A., and Trindade, R. I. F. (2015). The time dependence of reversed archeomagnetic flux patches. Journal of Geophysical Research: Solid Earth, 120:691–704.

Wardinski, I. and Lesur, V. (2012). An extended version of the C^3FM geomagnetic field model: Application of a continuous frozen-flux constraint. Geophysical Journal International, 189(3):1409–1429.